

Microcraters on Lunar Samples

H. Fechtig, W. Gentner, J. B. Hartung, K. Nagel,
G. Neukum, and E. Schneider
*Max Planck Institut für Kernphysik
Heidelberg, Germany*

D. Storzer
*Department of Mineralogy
Musée National d'Histoire Naturelle
Paris, France*

The lunar microcrater phenomenology is described. The morphology of the lunar craters is in almost all aspects simulated in laboratory experiments in the diameter range from less than 1μ to several millimeters and up to 60 km/s impact velocity. An empirically derived formula is given for the conversion of crater diameters into projectile diameters and masses for given impact velocities and projectile and target densities.

The production size frequency distribution for lunar craters in the crater size range from $\approx 1 \mu$ to several millimeters in diameter is derived from various microcrater measurements within a factor of up to 5.

Particle track exposure age measurements for a variety of lunar samples have been performed. They allow the conversion of the lunar crater size frequency production distributions into particle fluxes. These fluxes derived from lunar samples are consistent with satellite in-situ measurements. For example, for masses $m \geq (1 \pm 0.4) \times 10^{-12} \text{g}$, the latest HEOS satellite flux of $\phi = (7 \pm 2) \times 10^{-5} \text{m}^{-2} \text{s}^{-1}$ agrees with $\phi = (1 - 7) \times 10^{-5} \text{m}^2 \text{s}^{-1}$ derived from lunar data.

The development of crater populations on lunar rocks under self-destruction by subsequent meteoroid impacts and crater overlap is discussed and theoretically described. Erosion rates on lunar rocks on the order of several millimeters per 10^7 yr are calculated.

Chemical investigations of the glass linings of lunar craters yield clear evidence of admixture of projectile material only in one case, where the remnants of an iron-nickel micrometeorite have been identified.

Microcraters created as a result of hyper-velocity impacts of interplanetary particles are found on most lunar rock surfaces. In this respect the microcraters can be considered as micrometeoroid detectors exposed for geological periods of time.

It is the purpose of this presentation to outline the principal phenomenology of such craters and to give some synthesis of the investigations of a working group at the Max Planck Institut für Kernphysik, Heidelberg, which is concerned with crater statistics, laboratory cratering experiments, solar flare track exposure ages, calculations of inter-

planetary dust fluxes, erosion processes, and chemistry of craters (see also ref. 1).

Crater Phenomenology

Microcraters on silicate target materials consist of a central glass-lined depression (central pit; center of impact) embedded in a so-called spallation zone where target material is spalled off under the influence of a shock wave propagating in the course of the impact process. On glass targets the spallation zone tends to be circular and concentric

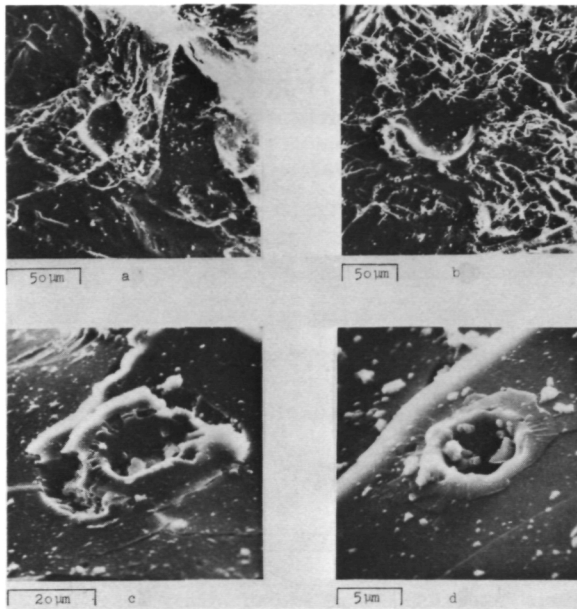


Figure 1.—Scanning electron microscope pictures of microcraters on lunar sample 12063,106. (a) and (b) Craters in crystalline material. (c) and (d) Craters in the glass linings of larger craters.

to the central depression. Spallation zones on crystalline material are mostly irregular in shape and may follow crystal structures or grain boundaries. Occasionally the material affected by the shock process is not completely thrown out of the spallation zone, but parts of it rest there slightly lifted above the undisturbed target surface (refs. 2 and 3). Examples of craters in glassy and crystalline lunar material are shown in figure 1.

In most cases larger craters ($\geq 50\text{-}\mu\text{m}$ central pit diameter) show a circular zone of higher albedo situated between the central pit and the spallation zone. This "halo zone" consists of finely fragmented material underlying the central pit. A crater with a prominent halo zone is displayed in figure 2.

In some cases the central pit is found to sit on some kind of a pedestal raised above the spallation level ("stylus pit"), or it may be not present at all ("pitless craters") (refs. 2, 4, and 5). An example of a stylus pit crater is given in figure 3, together with its laboratory-produced counterpart.

Microcraters on metal targets display only

a central pit, surrounded by a raised lip of "impact-fluidized" material (refs. 6 and 7). A similar behavior is found for very small ($\lesssim 1\text{-}\mu\text{m}$ diameter) craters on silicate material. The spallation zone is not present, and a depression looking very much like craters in metal targets remains. Often these craters are elongated, reflecting the obliquity of impact or irregularity of the impacting particle shape (ref. 8).

The morphology of microcraters on lunar samples can be simulated by laboratory experiments in almost all aspects (ref. 4). Figures 4 and 5 give a selection of lunar- and laboratory-produced craters with corresponding morphologies.

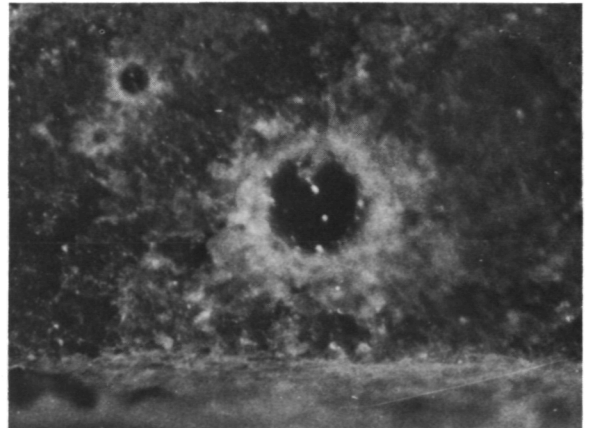


Figure 2.—Crater with prominent halo zone of higher albedo on lunar sample 60015,35 (central pit diameter $300\ \mu\text{m}$).

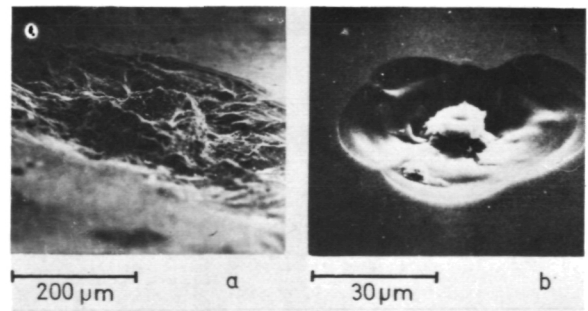


Figure 3.—"Stylus-Pit" craters. (a) Lunar sample 12024,8,1. (b) Laboratory produced crater, $3\ \text{km/s} < v < 5\ \text{km/s}$, $\text{Al} \rightarrow \text{quartz glass}$.

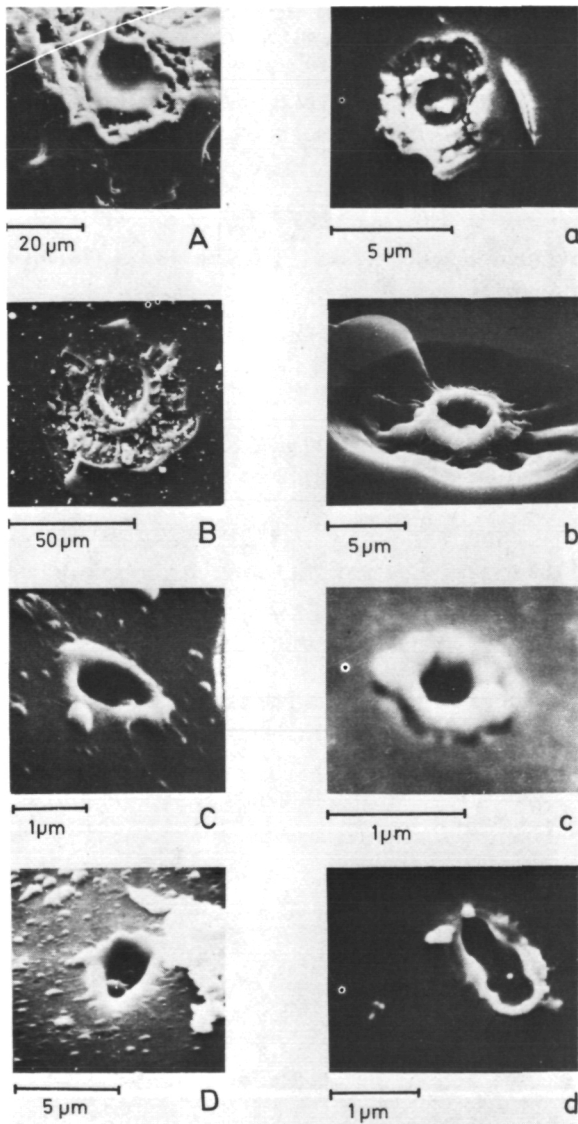


Figure 4.—Types of micron- and submicron-sized craters found on lunar samples, in comparison to craters produced in the laboratory. Lunar sample number: (A) 12063,106a Top (cryst. rock); (B) 14257 (coarse fines); (C) 14257 (coarse fines); and (D) 12063,106a Top (cryst. rock). Impact conditions: (a) Fe → Norite, $v = 7.6$ km/s; (b) Al → Quartz glass, $v = 5$ km/s; (c) Fe → Duran glass, $v = 50$ km/s; (d) Fe → Duran glass, $v = 30$ km/s, impact angle 45° .

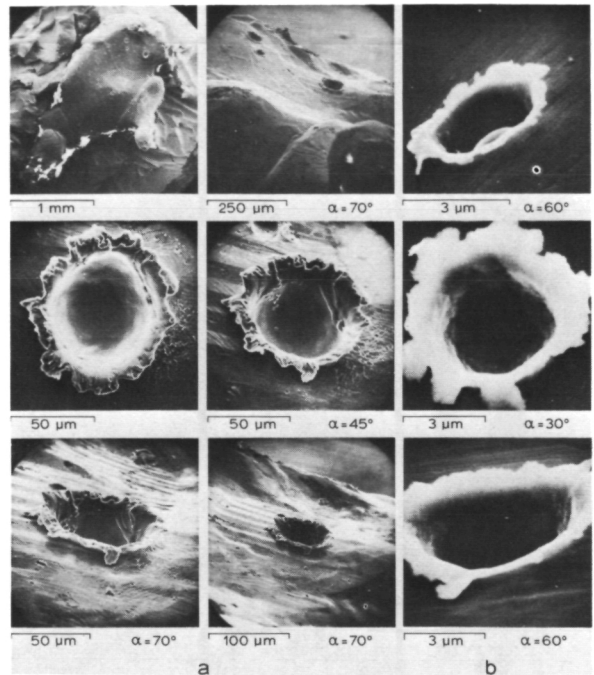


Figure 5.—(a, first two rows) Microcraters on Fe-Ni sample 60502,17 in comparison with (b, third row) laboratory-produced craters on metal targets (SEM-photographs, $\alpha =$ observation angle).

Laboratory Simulation Experiments

Using an electrostatic dust accelerator, projectiles in the mass range between 10^{-10} and 10^{-16} g were accelerated to velocities between 1 and 60 km/s (ref. 4). Using a lithium plasma gun, projectile masses between 10^{-5} and 10^{-8} g were accelerated to velocities between 2.5 and 18 km/s (ref. 9). Light gas gun projectiles of 10^{-2} g were accelerated to velocities between 1 and 4.5 km/s (ref. 10). Projectile materials were aluminum, carbon, iron, glass, and stainless steel, and target materials were glass, norite, stainless steel, aluminium, copper, and gold.

For both the dust accelerator and the light gas gun, it results for normal impacts occurring throughout the velocity range that the ratio of pit diameter to projectile diameter, D_P/d , is proportional to the two-thirds power of the impact velocity. Thus, $D_P/d \sim$

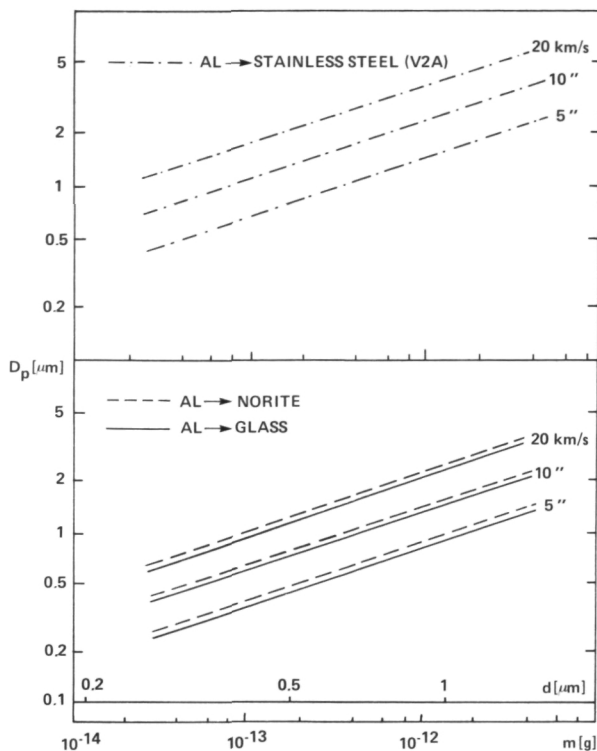


Figure 6.—Dependence of the central pit diameter, D_p , on projectile mass, m , or diameter, d , for different velocities. Data are for micron-sized aluminum projectiles impacting stainless steel, norite, and glass.

$v^{2/3}$. In figure 6, the dependence of D_p on d is given for different impact velocities.

Plasma gun experiments, however, produced mainly pitless craters. The ratio of the spallation zone diameter to projectile diameter, D_s/d , is proportional to the two-thirds power of the impact velocity; thus, $D_s/d \sim v^{2/3}$.

Though over-limited mass ranges, the experimental results can in each case be approximated by the two-thirds power laws, and the ratio D_p/d really slightly increases with increasing mass. From experiments showing pits, D_p/d increases a factor of 2 as projectile mass increases from 10^{-12} g to 10^{-2} g.

The ratio of the spallation zone diameter to projectile diameter, D_s/d , increases by a factor of 2 as projectile mass increases from 10^{-12} to 10^{-5} g. The ratio of the ki-

netic energy of the projectile to the volume of the crater is $E/v = 3.6 \times 10^{11}$ erg/cm³ for a projectile mass of 10^{-12} g, and $E/v = 4 \times 10^{10}$ erg/cm³ for a projectile mass of 10^{-2} g.

Using a formula from Gault (ref. 11) given for micrometer-to-centimeter-sized projectiles, these results can be represented approximately for normal impact over the whole experimental range from micron-sized to millimeter projectiles by slightly changing the constants

$$D_s = 10^{-3.077} \times \rho_t^{-1/2} \times \rho_p^{1/3} \times E^{1/2.65}$$

where ρ_t and ρ_p are target and projectile densities, respectively.

Crater Statistics

Cratered rock surfaces can display three categories of crater size frequency distributions.

As long as every impact crater on a surface exposed to the micrometeoroid bombardment is preserved, it is considered to be in the *production state*. The craters lie far apart and do not superpose one another. Figure 7 shows such a production crater population on a glass-coated lunar rock.

As time goes on, the crater frequency increases and crater superposition occurs; i.e.,

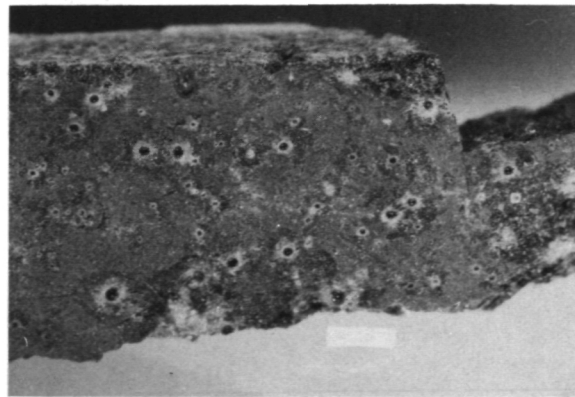


Figure 7.—Production crater population on lunar sample 60015,35. The light bar on top corresponds to 1 mm.

new impacts destroy already existing craters. The surface passes into a *transition state*. This process continues until on the statistical average the crater production rate is equal to the crater destruction rate and, therefore, the crater population remains constant. The surface has reached *crater equilibrium*.

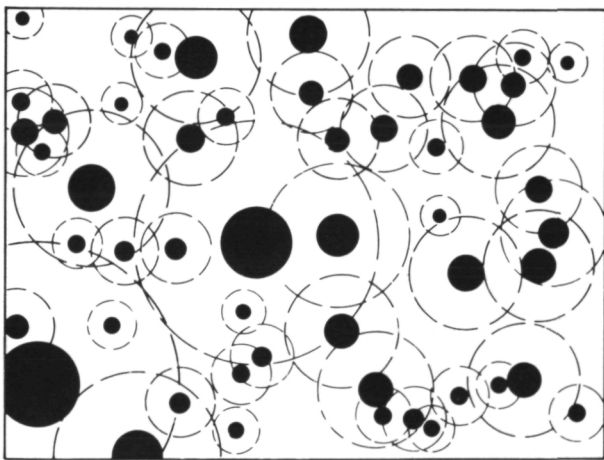
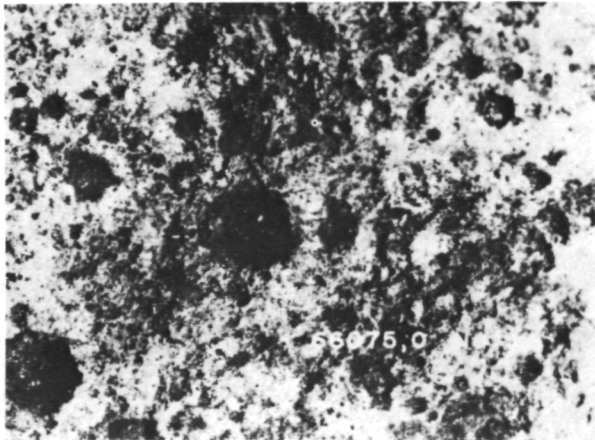


Figure 8.—Closeup photograph of rock 66075,0, considered to represent an equilibrium population. Width of frame approximately 1 cm). For comparison, a sketch depicting actual central pit locations and size (black dots) is added, and the actual, as well as eroded, spall zones (dashed circles) are indicated using the measured D_s/D_r value. Note the close proximity of many events, demonstrating that the effective destruction diameter operating in this surface is D_s . Note also the relative paucity of small events within the (somewhat younger) spall zone of the big crater in the center.

librium. An example of such a surface with a crater population in the equilibrium state is given in figure 8.

Figure 9 shows production size frequency distributions in the optically observable range of crater diameters. To eliminate exposure age differences, the curves are normalized at $D = 100 \mu\text{m}$, where $D =$ central pit

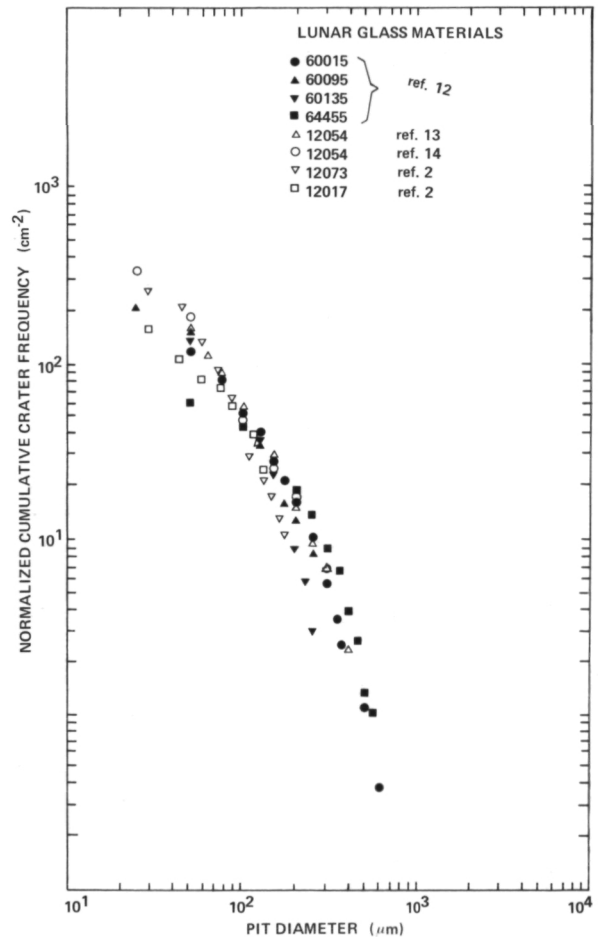


Figure 9.—Cumulative frequencies of microcraters obtained on a variety of glass surfaces representing production populations for microcraters with pit diameters $\geq 25 \mu\text{m}$. The consistent data for 12054 and 60015 are considered to be the most reliable because of the large number of craters counted in both cases. Note the relative steepening of the production slope at about $200\text{-}\mu\text{m}$ pit diameter, resulting in a production slope steeper than -2 . The curves are normalized at a pit diameter of $100 \mu\text{m}$.

diameter. The slopes for $D > 250 \mu\text{m}$ are grouping around -3 and steeper. The differences in slope are attributed to different exposure geometries of the individual lunar samples (ref. 12) and observational and statistical uncertainties. The flattening of the curves for $D < 250 \mu\text{m}$ is real, though somewhat exaggerated by observational losses in some cases and influenced by geometry effects. It means a depletion of craters of this size.

Figure 10 shows cumulative production state crater number densities in the micron and submicron size range, where only scan-

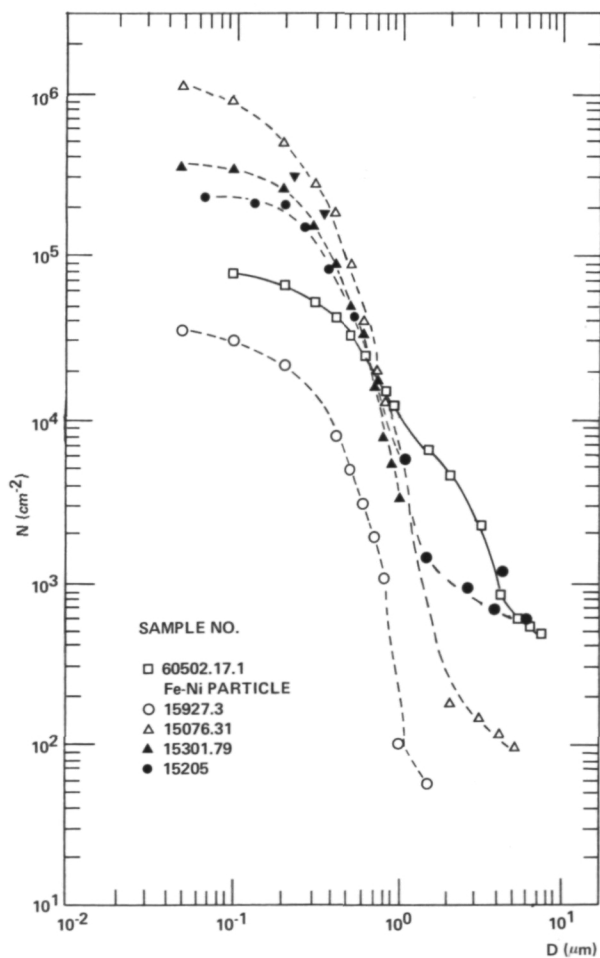


Figure 10.—Cumulative frequencies of micron-sized craters (production populations) as a function of the central pit diameter.

ning electron microscope investigations are feasible. These curves are not normalized and thus reflect differences in exposure age (ref. 6).

Measurements by different authors provide sufficient data to allow one to determine the production size distribution of microcraters on lunar rocks from less than 1μ to almost 1 cm in diameter. To derive the size distribution, we consider the following (1) Size distributions can usually be measured only in certain size ranges that depend on the size of a lunar rock, its exposure age, and the smoothness of its surface. (2) The absolute frequencies of craters in a certain size range vary with the exposure age of a rock. (3) In order to obtain the size distribution over the whole range of crater sizes observed on lunar rocks, normalization of microcrater frequencies derived from different measurements on different rocks is necessary. (4) The normalization range has to be chosen according to the quality of the data and the amount of overlap of the diameter ranges.

Figure 11 gives a compilation of currently available measurements of microcraters on lunar rocks, reduced in the above discussed way (ref. 17). The size distribution is determined within a factor up to 5. The slope is approximately equal to -2 in the micron-to submicron-size range; i.e., the distribution is steepening for $D < 1 \mu\text{m}$ (see also ref. 18). It is close to -1 in the range $1\mu\text{m} < D < 100 \mu\text{m}$. In the range $D > 300 \mu\text{m}$, the slope has been determined to have the value -3.6 ± 0.3 . Thus, the distribution steepens significantly for the millimeter-sized craters.

Another factor influencing crater statistics is the number of pitless craters that are mostly not accounted for. There is some evidence that the total number of pitless craters observed on cratered surfaces depends on mechanical surface properties, i.e., on the absolute crater frequency which controls the state of erosion. Although the statistics are relatively poor—eight data points for breccias and four data points for crystalline material—there is an indication that the number of pitless craters decreases with increasing areal crater density, an observation

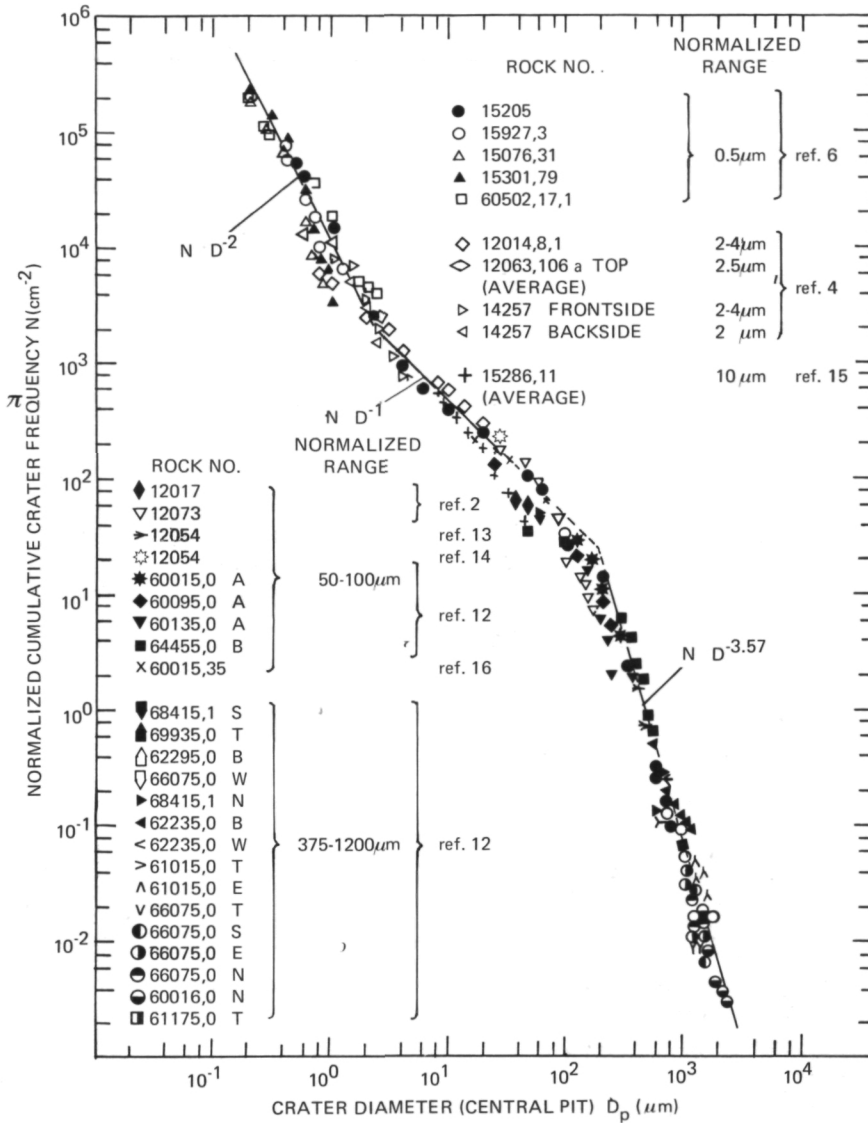


Figure 11.—Compilation of microcrater measurements of different authors. The frequencies are normalized at the ranges indicated (vertical shift of the distributions).

which can be explained in different ways. However, there is no unambiguous explanation yet available, so we prefer not to go into further details (see ref. 5).

Superposition of craters changes the slope of the crater distribution. For any production distribution slope steeper than -2 , it has been shown that the slope expected for the equilibrium crater population is -2 (ref. 19). In figure 12 the development of a crater

distribution with time is schematically shown. The longer the exposure time, t , the larger the craters affected by superposition. Thus, the production size distribution bends over to the equilibrium size distribution with the -2 slope for these sizes. With these assumptions, the tail of the distribution is always in the production state. It reflects the differences in exposure time. An alternative view also exists (ref. 20). Because rocks

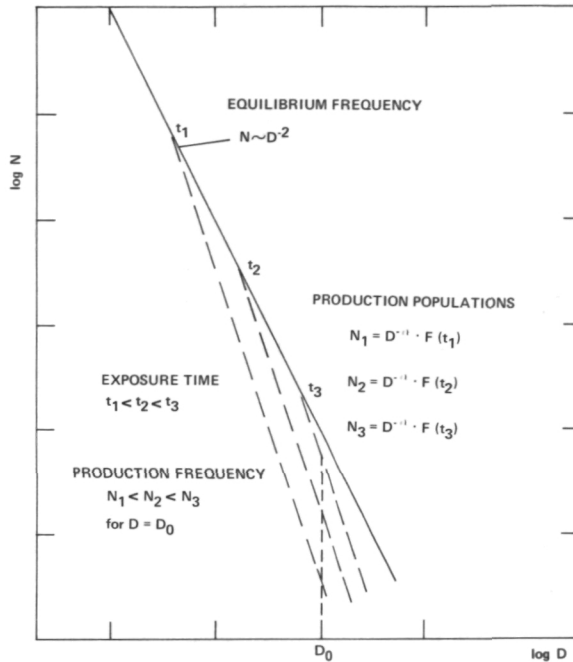


Figure 12.—Schematic display of the development of a crater population. Larger and larger craters are destroyed by superposition as time, t , goes on. The tail of the distribution remains in the production state, whereas small craters are in the equilibrium state.

destroyed early in their exposure lifetime are not collected by the astronauts, we can expect to recover a disproportionately large number of rocks which have survived longer than the expected mean lifetime. Thus, most rocks collected may not have received a representative share of larger craters and have enjoyed a statistical selection effect. Those large craters not accounted for would cause an artificial steepening of the cumulative size distribution curve. Therefore, lunar rock surfaces that have already reached an equilibrium state for small craters do not necessarily yield valid production distributions for larger craters. Shown in figure 13 is a hypothetical log-log cumulative size distribution diagram having a reference equilibrium line with a slope of -2 . Additional lines are shown that indicate how the observed distribution would appear for different numbers of unaccounted large craters due to the selection effect.

Figure 14 shows the behavior of real populations on lunar rocks (ref. 17). The picture is similar to the schematic treatment in figure 12. The difference in the frequencies at the tails of the distributions is greater than 10. The frequencies tend to become equal for smaller sizes where the slope is approximately equal to -2 . The difference between the highest and the lowest frequencies is less than a factor of 3. Ideally, the frequencies should be equal. This spread in the equilibrium frequencies is explained by different destruction conditions because of different ratios of spall sizes to pit sizes on different rocks (ref. 12), irregular spallation, and unobserved pitless craters. Additionally, the low-frequency populations might be still in the transition state.

Quantitatively, the equilibrium frequency N_E is written as $N_E = A \times D^{-2}$, where the

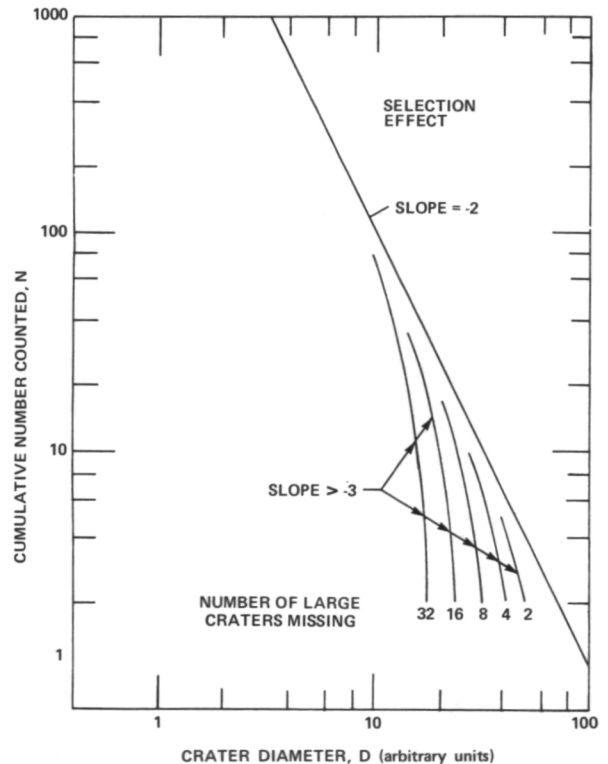


Figure 13.—Diagram illustrating the steepening of an equilibrium size distribution curve due to selection effects.

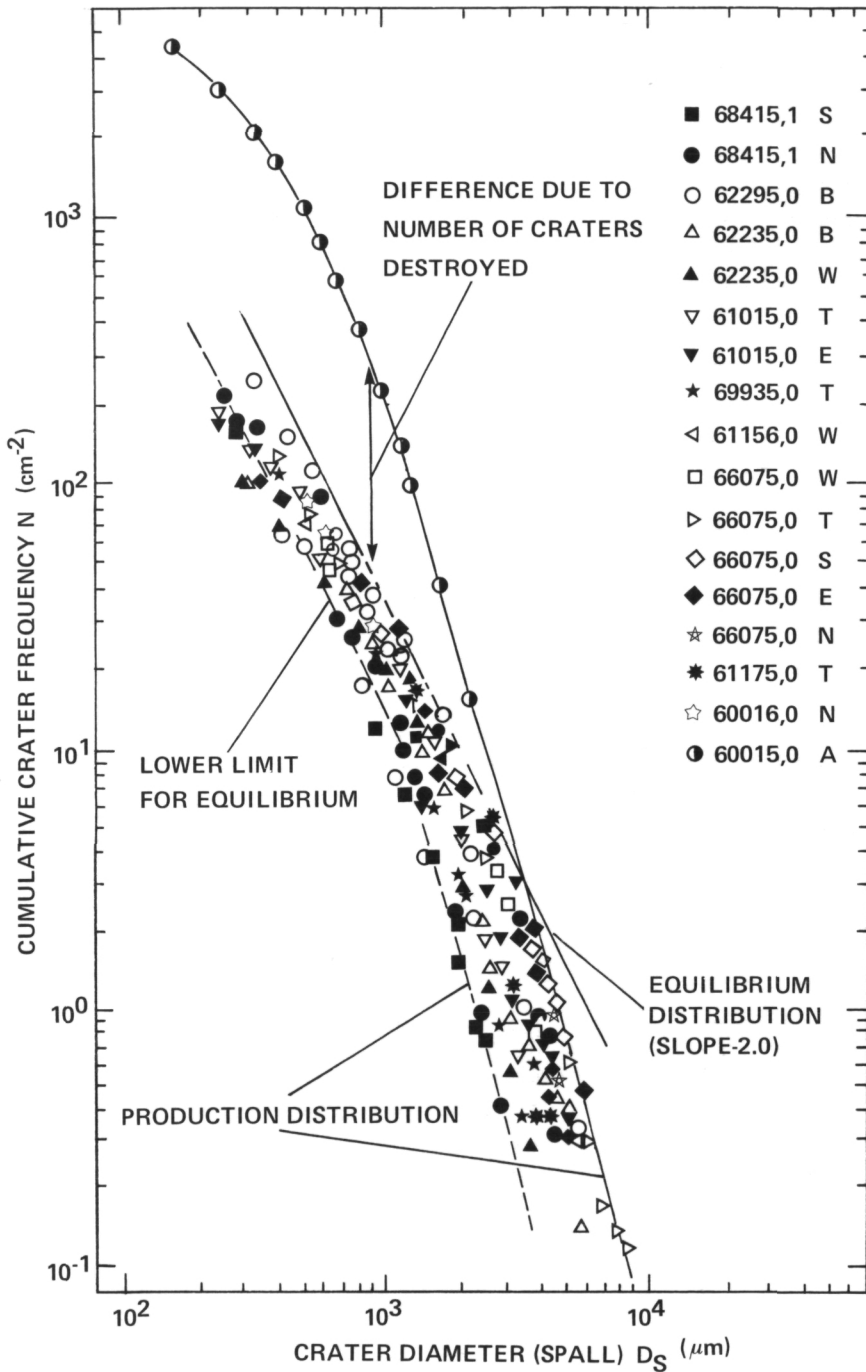


Figure 14.—Compilation of microcrater distributions measured on Apollo 16 rocks (ref. 12). The smaller craters are in the equilibrium state. The frequency variation in this range (a factor ≤ 3) is due to different destruction depending on different D_s/D_p ratios and rock properties. The large craters (steep slope) are in the production state. The number of craters destroyed is indicated by comparison with the extrapolated production distribution derived from the distribution on sample 60015,0.

crater diameter D can be either the spallation diameter D_s or the pit diameter D_p . The areal density coefficient, A , is expressed in the following way:

$$A = \frac{2 \times (\alpha - 2)}{\pi} \left(\frac{D_p}{D_s} \right)^{\alpha-2}$$

where $-\alpha$ is the slope of the production population in the $\log N$ versus $\log D$ plot. The D_p/D_s ratio is generally smaller on crystalline rocks than on breccias. Thus, one has to expect a corresponding variation in absolute equilibrium crater frequencies as is demonstrated in figure 14.

The highest frequencies we found on lunar rocks are limited by the above-discussed processes. Maximum crater number densities found per square centimeter are 100–150 for $D_p \geq 100 \mu\text{m}$; 3000 for $D_p \geq 1 \mu\text{m}$; 10^6 for $D_p \geq 0.1 \mu\text{m}$ (refs. 6 and 12).

As discussed above, the density of craters can be expressed independent of size if the crater distribution follows the law $N = A \times D^{-2}$. This is valid for populations in equilibrium and for the range $D_p < 250 \mu\text{m}$ as a tangential relationship for any lunar microcrater population because the slope flattens for smaller sizes.

Maximum measured areal density coefficients for a number of different rocks with different physical properties are plotted in figure 15, together with the limiting frequency value of Morrison et al. (ref. 21). Gault's (ref. 22) saturation percent values are given for comparison with the areal density coefficient values (ref. 12). We find, especially for the Apollo 16 rocks, a wide range of crater densities. Low maximum values for "glass" surfaces occur because we measured essentially populations in the production state. Other populations with similar values may be considered also in production, provided D_s/D_p is the same, and excessive numbers of pitless craters do not exist.

Regarding the higher areal density values, we have concluded that these populations are in or approaching the equilibrium state. We find no simple relationship between areal density values for populations close to equilibrium and physical properties of the rocks.

In general, however, crystalline rocks seem to have lower maximum densities than breccias.

Exposure Ages

In order to convert crater populations on a given sample into the interplanetary dust flux, the sample's residence time at the lunar surface must be known. Therefore, solar flare exposure ages were determined for samples 15076,31; 15015,24; 15927,3; 15301,79; 15205,51,1; 60502,17; 60015,35; and a glass-lined crater pit found in the Luna 16 core (C 19.118; 20–22 cm). For track observation, both optical and scanning electron microscopy were used. Detailed procedures are described elsewhere (ref. 23).

In all but samples 15076 and 60015 the depth dependence of solar flare tracks was studied in the glass phase. In lunar glasses the solar flare tracks are annealed to a con-

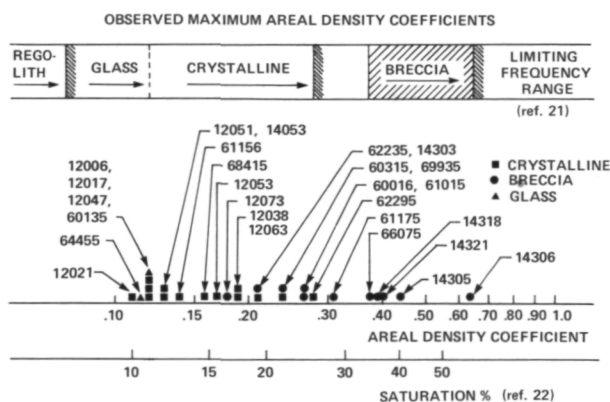


Figure 15.—Comparison of highest areal density coefficients observed to date on various lunar surface materials. Only the highest densities are plotted. Note the systematic difference of the areal density coefficients for various lunar rocks. These differences may be attributed to exposure age, rock properties, or a combination of both. The areal density coefficients for glass do not necessarily mean the highest approachable densities because only production populations have been investigated. For comparison, coefficients for loose regolith are indicated. Also shown are saturation percent values defined by Gault (ref. 22).

siderable extent (refs. 4 and 24). Accordingly, the track sizes are diminished and the track densities reduced (ref. 24). However, this very fact allows accurate track counting in a sample's near-surface, high-track density region and evaluation of the depth dependence of solar flare tracks. Thereafter, the track densities were corrected according to the respective size shrinkage of the track etch pits (ref. 24) and/or normalized to the track densities of pyroxenes that were trapped within the glass phases.

In all samples studied (except sample 60502, probably due to a 100- μ m Ni-Fe cover) the track densities P decrease with depth R from the surface according to $P = \text{const} \times R^{-\alpha}$. The α -values range between 2.5 and 2.8 (ref. 23), agreeing well with the track record of the uneroded Surveyor III glass lens (refs. 25, 26, and 27). We therefore conclude that erosion affected our samples only to a minor degree. Furthermore, the surfaces were irradiated and cratered having a solid angle of exposure of essentially 2π . The solar flare exposure ages are compiled in table 1. For their calculation, track production rates based on the revised Surveyor III track record were used (ref. 23). (In an earlier paper, ref. 6, the track production rates used were different and the ages therefore lower.) The Surveyor III spacecraft was on the Moon during the period of maximum solar activity and for a fraction of the present solar cycle only. On the other hand, the flux data have not to be representative for the long time averaged solar activity. This uncertainty in applying

the Surveyor III record to our lunar samples results in an age uncertainty of about a factor of 2.

Among charged particle track exposure ages of lunar rock surfaces determined by different groups, there exist some apparent systematic discrepancies up to a factor of 3. This might be due to an insufficient calibration and standardization of the particle track method. For example, there exists a difference in the etchable ranges of tracks in the various detectors used (glasses, feldspars, or pyroxenes), differences in the track etching conditions applied (etchant, temperature, and etching time), and differences in the track observation technique (optical, scanning electron, or transmission electron microscopy).

Particle track exposure ages have been determined by different authors for a variety of Apollo 12, 14, 15, and 16 rocks, where mostly millimeter-sized craters have been measured. As seen before, the size distribution in this range follows the law $N \sim D_p^{-3.57}$ on the average, or in terms of spall diameters, $N = Q \times D_s^{-3.57}$. Normalized to crystalline rock, we obtain $N_{\text{norm}} = Q_{\text{norm}} \times D_s^{-3.57}$, where $Q_{\text{norm}} = q^{3.57} \times Q$. The factor q is the ratio of D_s/D_p for crystalline rock and D_s/D_p for the special rock whose crater population is measured: $q = \frac{D_s(\text{cryst.})}{D_s(\text{meas.})}$. It is assumed that for the same impact on different rocks with different composition and texture (e.g., breccias compared to crystalline rocks), the central pit with diameter D_p has the same size, but the ratio of spall diameter to pit

Table 1.—*Exposure Ages Determined by Means of Solar Flare Tracks*

Sample number	15015, Luna 24 ⁽¹⁾ 16 ⁽¹⁾	15927,3	15205, 51,1	15301, 79	15076, 31	60502,17 ⁽²⁾	60015,35
Solar flare exposure age	40 5.7×10^3	4.8×10^3	7.9×10^4	9.6×10^4	2.6×10^5	1.1×10^4	1.5×10^5

NOTES: (1) No microcraters have been found on these samples.

(2) Considering the higher stopping power of iron, we corrected our data to an equivalent shielding of stony material.

diameter, D_s/D_p , is different. The time integral of the cumulative crater production rate $\phi(D)$ gives $N = \phi(D) \times t_A = \text{const} \times t_A \times D_s^{-3.57}$ (time constant influx assumed). Thus it results after normalization (a) for $D_s = 1 \text{ mm}$

$$N_{\text{norm}} = c_1 \times t_A$$

or

(b) $Q_{\text{norm}} = c_2 \times t_A$, independent of D_s .

Particle track exposure ages of dated rocks are plotted against the respective crater frequency measurements in terms of N_{norm} ($D_s = 1 \text{ mm}$) and Q_{norm} in figure 16. The data can be fitted by the expression

$$t_A = 7.3 \times 10^7 \times Q_{\text{norm}}$$

respectively,

$$t_A = 2.10^4 \cdot N_{\text{norm}} \quad (D_s = 1 \text{ mm})$$

which would correspond to a time constant influx between roughly 3×10^5 and 3×10^6 yr ago. These formulae can be used to determine exposure ages by crater statistics that correspond to particle track ages.

A different view is presented by Hartung et al. (ref. 20). The correlation shown in figure 16 may be independent of time because both solar flare tracks and microcraters occur at the surfaces of lunar rocks. Thus, rocks having physical properties permitting a higher erosion rate would have lower track and crater densities at the surface. The correlation observed then reflects different physical properties of rocks rather than different exposure ages.

Meteoroid Fluxes

Using the following formula it is possible to calculate the meteoroid flux ϕ for a production crater population with known exposure time.

$$\phi = \frac{N}{t} \quad (1)$$

where ϕ = meteoroid flux per m^2s

N = cumulative crater number per m^2

t = exposure time

Knowing the impact velocity, the conversion of crater diameters into particle diameters is accomplished with the help of the simulation results. However, the results obtained in this way are for an isotropic spatial distribution. The results of recent space probe and satellite measurements show, however, a rather strong anisotropy in spatial distribution.

The Pioneer 8/9 dust experiment (ref. 35) shows that a sensor orbiting the Sun at 1 AU and spinning in the ecliptical plane is hit by two major dust streams, one from the apex direction (direction of Earth's motion around the Sun) and one from the direction of the Sun. Contrary to the apex particles, the Sun particles are the most frequent ones in terms of event rates. Although it was not possible to measure particle mass and impact velocity separately, there is strong evidence that these particles are extremely small ($< 1 \mu\text{m}$ in diameter), and the impact velocity is higher compared to the apex particles. The impact velocity is considered to be higher than 50 km/s and may even exceed 100 km/s (ref. 35), depending on particle diameter. Zook and Berg (ref. 36) propose that these submicron-sized particles are being produced from normal zodiacal dust particles. These zodiacal dust particles, following the Poynting-Robertson effect (ref. 37), are continuously losing energy and thus spiraling into the Sun. In the neighborhood of the Sun the particles partly melt and/or are fragmented by collisions. As a result of these processes, submicron-sized fragments are accelerated by the radiation pressure and blown out of the solar system on hyperbolic orbits. Hemenway et al. (ref. 38) claim, however, that submicron-sized particles may come off the surface of the Sun and may be blown out of the solar system.

The HEOS 2 dust experiment (refs. 39 and 40) is measuring the dust population in apex, anti-apex, ecliptic north, and ecliptic south directions. It has shown that the apex flux is the most dominant flux. The fluxes in the other directions are approximately 2 orders of magnitude lower compared to the apex flux. The impact velocities of the apex

particles show a broad distribution, from 2 km/s (sensitivity barrier) up to about 25 km/s, and averaging at about 10 km/s. These results are in agreement with results from the Pioneer 8/9 dust experiment (ref. 41), and the velocity distribution is expected as a consequence of the Poynting-Robertson effect.

In conclusion, one can state from the latest in-situ measurements that the Moon is hit by the apex-particle flux for particles $\gtrsim 1 \mu\text{m}$ in diameter at 10 km/s impact velocity and by the Sun-particle flux for particles $\lesssim 1 \mu\text{m}$ in diameter at $> 50 \text{ km/s}$ impact velocity.

Concerning the crater size distributions,

Schneider et al. (ref. 6) have reported a bimodal distribution in crater sizes. Let us assume that the micron-sized and larger craters have been produced by apex particles and the submicron-sized craters by sun particles. It is then possible to convert the crater sizes into the respective particle sizes. For 10 km/s impact velocity, D_P/d is between 1.4 and 2 for crater diameters D_P between $1 \mu\text{m}$ and 1 mm. For 50 km/s impact velocity and crater diameters $< 1 \mu\text{m}$, D/d is 4 for glass targets and 7 for metal targets as shown in figure 6. The conversion into fluxes is then accomplished applying formula (1) to the respective production crater distribu-

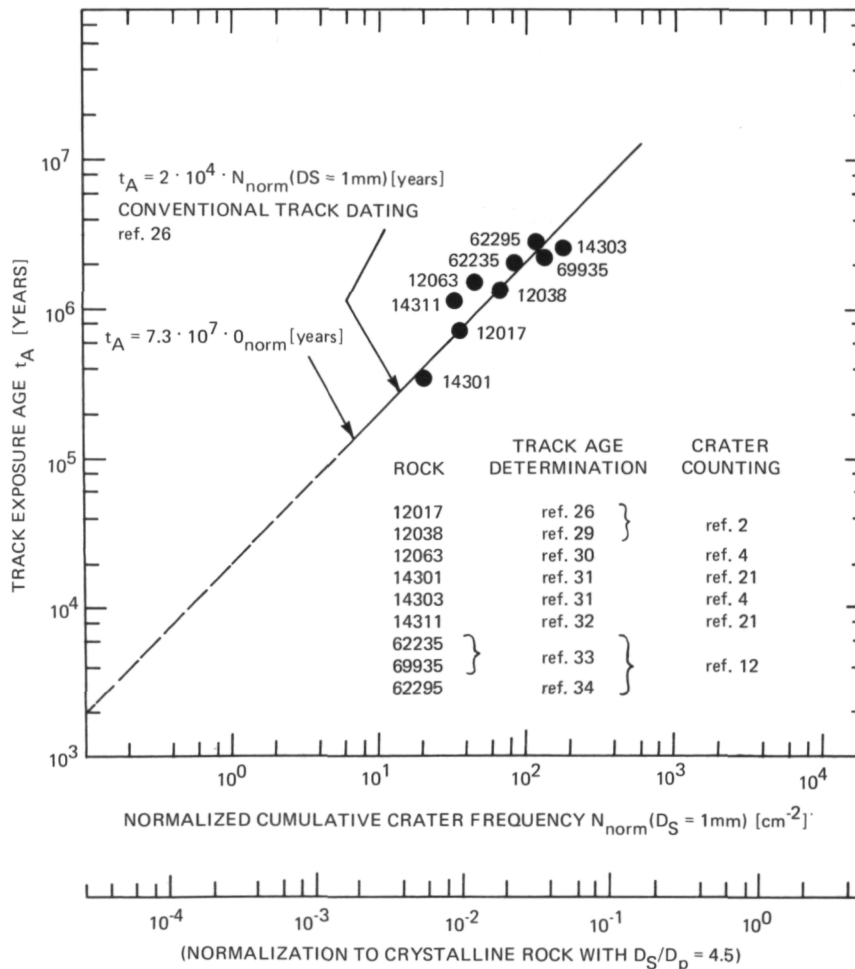


Figure 16.—Relationship between particle track exposure ages of individual lunar rocks and the microcrater production frequencies (tails of the distributions) measured on them.

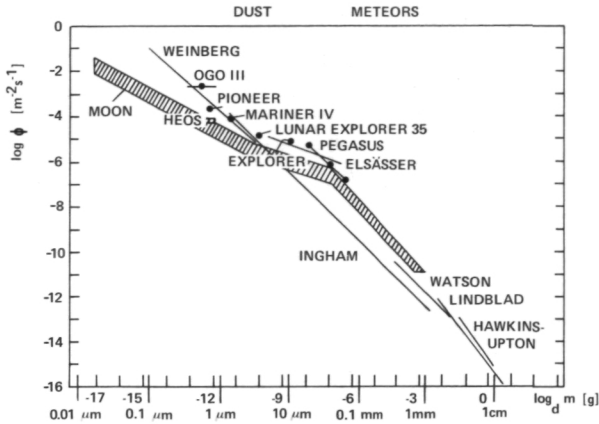


Figure 17.—Comparison of micrometeoroid fluxes derived from lunar microcrater measurements with those obtained in various satellite in-situ experiments.

tion. Since the Moon is a spinning Earth satellite, the surface is hit by the dust streams only part of the time. The results, therefore, have to be multiplied by the factor of π , if unidirectional fluxes are concerned.

The final flux results are given in figure 17. The numbers of dust particles are cumulatively plotted as a function of particle mass. The results obtained from lunar microcrater statistics are labeled "Moon." This is the time-averaged flux on a lunar surface exposed directly to the two major dust streams while the Moon rotates and orbits the Sun with the Earth (ref. 16).

In comparison with other flux results given in the flux diagram, it seems that the Moon flux is lower. However, all measurements with exception of the HEOS value are calculated under the assumption of a 2π -steradian detector exposure geometry and an isotropic flux direction. As discussed above, this assumption has to be revised drastically. For a two-stream particle flux distribution, the HEOS flux comes close to the Moon flux. This suggests that the present meteoroid flux is nearly the same as that averaged over more than 10^5 yr.

Results contrary to this have been obtained based on solar flare track exposure age measurements of individual lunar micro-craters (ref. 42). The age distribution of micro-

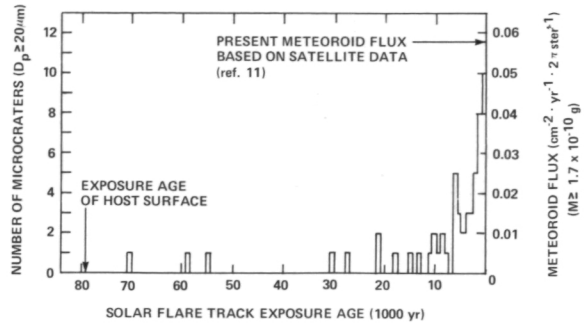


Figure 18.—Solar flare track exposure age measurements of single microcraters ($D_p \geq 20 \mu\text{m}$) on sample 15205,51.

craters found in this way suggests that a higher flux exists now compared with that existing at any time during the last 100 000 yr (fig. 18). Further measurements are needed to explain this discrepancy.

Erosion of Lunar Rocks

Erosion of lunar rocks is dominantly controlled by micro-meteorite impact, which is a random process. Analytical model calculations yield only statistical averages. However, for most applications in lunar rock analysis it is of interest how a rock surface topography develops under continuous meteorite bombardment; deviations from averages and the uniqueness of single-spot exposure histories have to be taken into account. Therefore, a Monte Carlo computer model has been worked out (ref. 43). A given test area was randomly covered with craters of 17 size classes.

The total simulated crater diameter interval extends from $152 \mu\text{m}$ to 2.4 cm in spall diameter. This range contributes dominantly to the abrasion of rocks sampled during the Apollo missions.

The probabilities for the occurrence of different crater sizes were calculated on the basis of production state crater distributions actually observed on lunar sample surfaces.

The test area itself was subdivided into roughly 27 000 area elements (cells), which

were characterized by their center coordinates. The computer kept track of the erosion state, i.e., the depth level of each area element. Some of the main results of this computer model are as follows.

Figure 19 gives the percentages of surface area affected (i.e., number of area elements affected) as a function of total numbers of craters produced. Notice that already after about 8300 craters 50 percent of the total area has been affected, whereas it takes another 70 000 to 80 000 craters to completely cover the remaining 50 percent. With increasing model time the probability for one cell's being affected repeatedly by impacts is increasing, too. The curves in the lower part of the diagram represent these multi-impact percentages of the surface. For ex-

ample, after 100 000 craters have been produced, about 5 percent of the surface will have been impacted not less than 11 times.

Figure 20 illustrates the maximum deviations of certain coherent reference areas from the average erosion depth of the whole surface, again as a function of total crater numbers or model time. Depending on the size of the reference area there may easily occur deviations up to factors of 10 in both directions, which means that small sample chips, usually available for laboratory investigations, cannot be considered as being representative for whole sample surfaces.

If one applies different crater production rates derived from model fluxes of the interplanetary dust (figure 17), the model results can be related with absolute times, and aver-

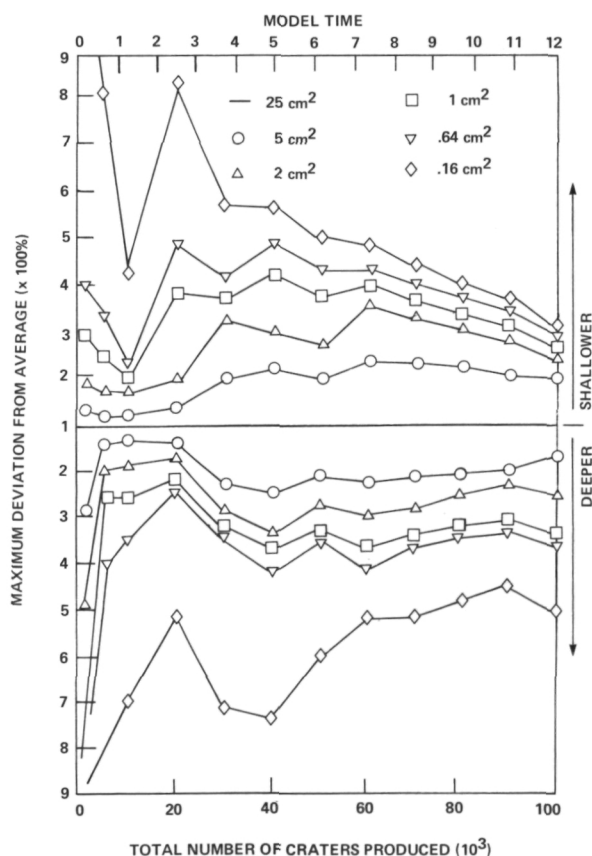


Figure 19.—Percentages of surface area affected X many times (X = 1,2,3...) as a function of total number of impacts produced.

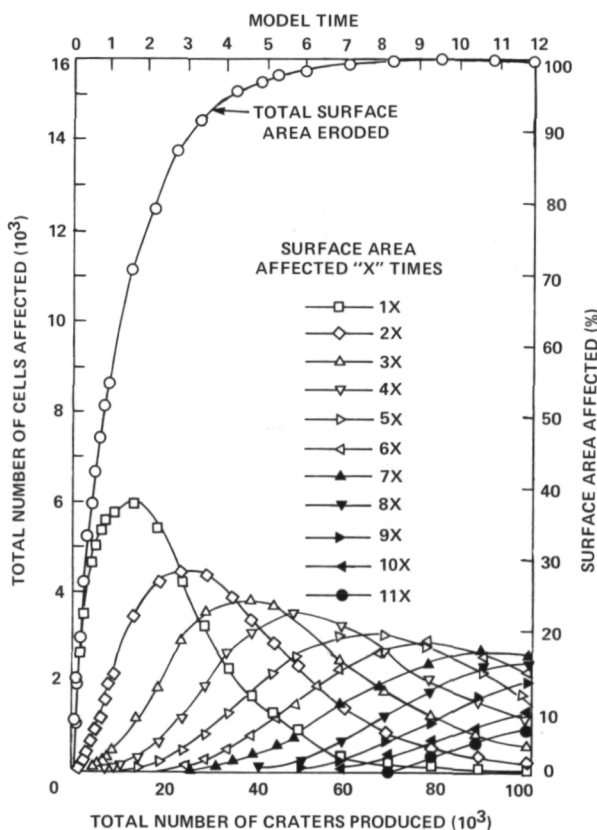


Figure 20.—Maximum deviation from the average erosion depth of the whole test surface plotted against model time for different reference areas.

age erosion rates can be determined. They range roughly between 0.07 mm and 0.7 mm per 10^6 yr.

Erosion rates (single particle abrasion) can be calculated analytically. The mass ejection M_e per impact with mass m at 20 km/s impact velocity can be derived from a formula by Gault (ref. 44), resulting in $M_e = 10^{3.575} \times m^{1.133}$. Following a procedure by Gault et al. (ref. 44), erosion rates of 0.1 to 0.3 mm per 10^6 yr are calculated (ref. 17). This value is dependent on the crater production rate used. In this case, a rate consistent with the data in figure 17 is used.

Chemistry

The glass lining of lunar microcraters has been investigated for admixture of projectile material with an electron microprobe. Detailed analyses of several craters on the glass coating of sample 60015,35 and of one crater on the crystalline sample 12002,100 have been performed.

The coating of 60015 was initially glass a few millimeters thick, but has devitrified to elongate plagioclase crystals with 2- to 50- μ dimensions and pyroxene-composition interstitial material. Point electron microprobe analyses for Fe, Mg, Ca, Al, and Si of glasses lining several 100- μ -sized pits show no indication of material in the pit glasses that is outside the range in composition of the host sample phases. Either the projectile material composition is similar to the host material composition, or little or no projectile material remained in the pit glass in these cases.

Similar measurements that suggest some presence of projectile material or fractional vaporization during the impact process have been performed by Mehl (ref. 45).

A 0.5 mm pit on sample 12002,100 showed numerous mounds associated with its glass coating. The mounds consist of mainly iron and nickel, with an iron-to-nickel ratio of 20:1. This indicates that the mounds are the remnants of an iron-nickel micrometeoroid that formed this crater (ref. 16). Figure 21 shows the distribution of iron and nickel in

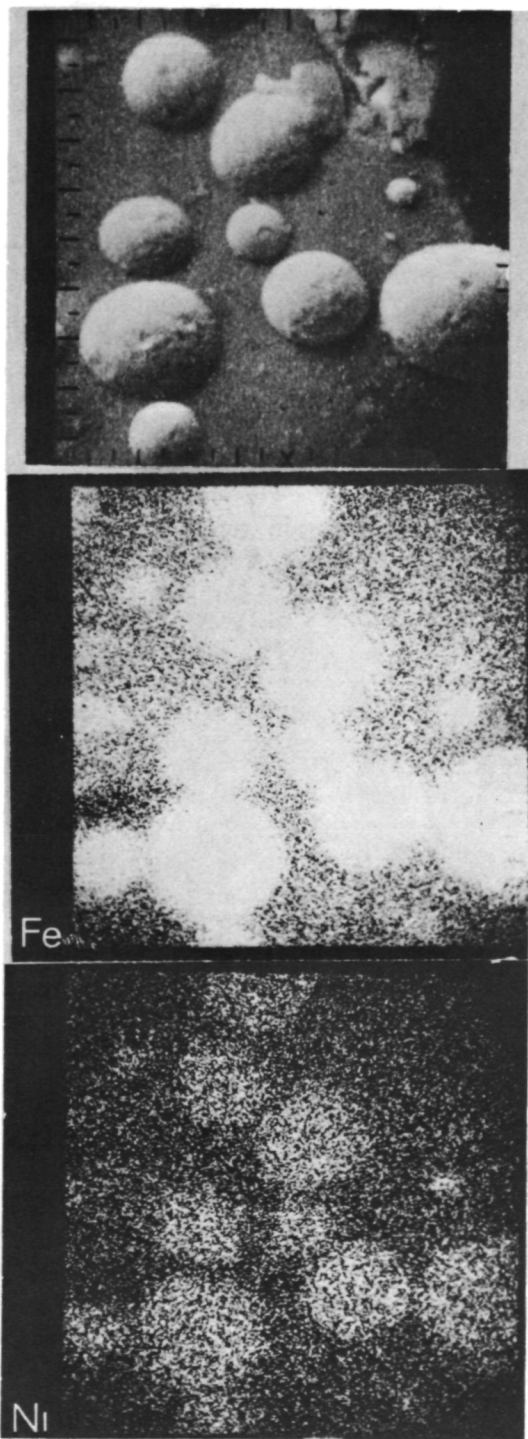


Figure 21.—Nickel-iron mounds in a 500- μ m crater on sample 12002,100. Microprobe secondary electron scanning picture with corresponding Fe-K α and Ni-K α X-ray scanning images (frame width $\approx 30 \mu\text{m}$).

the mounds and the surrounding crater glass lining.

Conclusions

The lunar microcrater phenomenology has been simulated in laboratory experiments in almost all aspects. Additionally, the laboratory experiments allow the conversion of crater diameters into projectile diameters and masses at given impact velocities and projectile and target densities. These experimental results are applied to lunar microcrater populations.

Various measurements of microcrater production size frequency distributions exist in different size ranges. A compilation of these data yields the size frequency distribution for the diameter range between 1 μm and 1 mm, with an uncertainty of up to a factor of 5.

The time development of crater population is qualitatively understood. The crater populations start as production populations, where essentially no craters have overlapped and destroyed each other. As time goes on, crater destruction occurs by subsequent crater superposition. The populations pass through a transition state, where the crater distributions are gradually deviating from the production distributions. Finally, an equilibrium state is reached: on the statistical average, the number of craters in this state does not change. Theoretical descriptions of the equilibrium state satisfactorily agree with the observational data.

Surface exposure ages have been determined from particle track measurements. The flux of interplanetary dust impacting the surface of the Moon is obtained by correlating areal crater densities with surface exposure ages. Such a correlation observed for large craters ($100 < D_p \lesssim 1000 \mu$) on surfaces approaching equilibrium with respect to cratering may be a basis for a flux determination or, alternatively, an exposure time measurement if the flux (or the crater production rate) is known. Another interpretation of such a correlation is that since

both solar flares and microcraters occur at the exposed lunar surface, they both suffer the same effects of erosion, and the correlation observed reflects only the relative "erodability" of different samples.

The latest in-situ micrometeoroid measurements are important for the interpretation of the lunar crater frequencies: two major dust streams are hitting the Moon from distinct spatial directions—apex and Sun; the correspondent impact velocities are about 10 km/s for the apex dust stream and about 50 km/s for the Sun dust stream.

Taking into account the spin of the Moon relative to the Sun, it is possible to calculate a unidirectional flux valid for the Moon. This flux is fairly consistent with recent in-situ measurements, considered under the same conditions (Pioneer 8/9 and HEOS 2 results). On the contrary, Hartung et al. (ref. 42) have found an increased flux at present from individual microcrater glass linings dated by means of solar flare track measurements. Further measurements are necessary to resolve this discrepancy.

Monte Carlo computer simulation and analytical treatment of the erosion of lunar rocks by micrometeoroid impacts lead to consistent erosion rates of several millimeters per 10^7 yr.

Measurements of the chemical composition of the glass linings of several craters $\gtrsim 100 \mu\text{m}$ in diameter yielded the unambiguous presence of projectile material only in one case, where the remnants of an iron-nickel micrometeorite have been detected.

Acknowledgment

Appreciation is expressed for the financial support provided to D. Storzer by the Deutsche Forschungsgemeinschaft.

References

1. HÖRZ, F., D. E. BROWNLEE, H. FECHTIG, J. B. HARTUNG, D. A. MORRISON, G. NEUKUM, E. SCHNEIDER, AND J. F. VEDDER, Lunar Microcraters, Implications for the Micrometeoroid

- Complex. *Planet. Space Sci.*, in press, 1974.
2. HÖRZ, F., J. B. HARTUNG, AND D. E. GAULT, Micrometeorite Craters and Lunar Rock Surfaces. *J. Geophys. Res.*, Vol. 76, 1971, pp. 5770-5798.
 3. BLOCH, M. R., H. FECHTIG, W. GENTNER, G. NEUKUM, AND E. SCHNEIDER, Meteorite Impact Craters, Crater Simulation, and the Meteoroid Flux in the Early Solar System. *Proc. Second Lunar Science Conference, Geochimica et Cosmochimica Acta*, Supplement 2, Vol. 3, 1971, pp. 2639-2652.
 4. NEUKUM, G., E. SCHNEIDER, A. MEHL, D. STORZER, G. A. WAGNER, H. FECHTIG, AND M. R. BLOCH, Lunar Craters and Exposure Ages Derived From Crater Statistics and Solar Flare Tracks. *Proc. Third Lunar Science Conference, Geochimica et Cosmochimica Acta*, Supplement 3, Vol. 3, 1972, pp. 2793-2810.
 5. SCHNEIDER, E., AND F. HÖRZ, Microcrater Populations on Apollo 17 Rocks. *Icarus*, in press, 1974.
 6. SCHNEIDER, E., D. STORZER, J. B. HARTUNG, H. FECHTIG, AND W. GENTNER, Microcraters on Apollo 15 and 16 Samples and Corresponding Cosmic Dust Fluxes. *Proc. Fourth Lunar Science Conference, Geochimica et Cosmochimica Acta*, Supplement 4, Vol. 3, 1973, pp. 3277-3290.
 7. RUDOLPH, V., Untersuchungen an Kratern von Mikroprojektilen im Geschwindigkeitsbereich von 0.5-10 km/s. *Z.f. Naturforschung*, Vol. 24a, 1969, pp. 326-331.
 8. BROWNLEE, D. E., F. HÖRZ, J. F. VEDDER, D. E. GAULT, AND J. B. HARTUNG, Some Physical Properties of Micrometeoroids. *Proc. Fourth Lunar Science Conference, Geochimica et Cosmochimica Acta*, Supplement 4, Vol. 3, 1973, pp. 3197-3212.
 9. NAGEL, K., *Experimente zur Kratersimulation*. Master's Thesis, Universität Heidelberg, 1973.
 10. SCHNEIDER, E., *Mikrokrater auf Mondgestein und deren Laborsimulation*. Ph.D. Thesis, Universität Heidelberg, 1972.
 11. GAULT, D. E., F. HÖRZ, AND J. B. HARTUNG, Effects of microcratering on the lunar surface. *Proc. Third Lunar Science Conference, Geochimica et Cosmochimica Acta*, Supplement 3, Vol. 3, 1972, pp. 2713-2734.
 12. NEUKUM, G., F. HÖRZ, D. A. MORRISON, AND J. B. HARTUNG, Crater Populations on Lunar Rocks. *Proc. Fourth Lunar Science Conference, Supplement 4, Vol. 3, 1973, pp. 3255-3276*.
 13. HARTUNG, J. B., F. HÖRZ, AND D. E. GAULT, Lunar Microcraters and Interplanetary Dust. *Proc. Third Lunar Science Conference, Geochimica et Cosmochimica Acta*, Supplement 3, Vol. 3, 1972, pp. 2735-2753.
 14. NEUKUM, G., *Untersuchungen über Einschlagskrater auf dem Mond*. Ph.D. Thesis, Universität Heidelberg, 1971.
 15. BROWNLEE, D. E., F. HÖRZ, J. B. HARTUNG, AND D. E. GAULT, Micrometeoroid Craters Smaller Than 100 Microns. *The Apollo 15 Lunar Samples*, Lunar Science Institute, Houston, 1972, pp. 407-409.
 16. FECHTIG, H., J. B. HARTUNG, K. NAGEL, G. NEUKUM, AND D. STORZER, Microcrater Studies, Derived Meteoroid Fluxes and Comparison With Satellite-Borne Experiments. *Lunar Science*, Vol. V Abstracts pp. 222-224; *Proc. Fifth Lunar Science Conference, Geochimica et Cosmochimica Acta*, Supplement 5, Vol. 3, in press, 1974.
 17. NEUKUM, G., *The Interaction of Micrometeoroids With Lunar Rocks*. To be published, 1974.
 18. BLANFORD, G., D. MCKAY, AND D. MORRISON, Accretionary Particles and Microcraters. *Lunar Science*, Vol. V Abstracts, Part 1, 1974, pp. 67-69.
 19. NEUKUM, G., AND H. DIETZEL, On the Development of the Crater Population on the Moon With Time Under Meteoroid and Solar Wind Bombardment. *Earth Planet. Sci. Letters*, Vol. 12, 1971, pp. 59-66.
 20. HARTUNG, J. B., F. HÖRZ, F. K. AITKIN, D. E. GAULT, AND D. E. BROWNLEE, The Development of Microcrater Populations on Lunar Rocks. *Proc. Fourth Lunar Science Conference, Geochimica et Cosmochimica Acta*, Supplement 4, Vol. 3, 1973, pp. 3213-3234.
 21. MORRISON, D. A., D. S. MCKAY, H. J. MOORE, AND G. H. HEIKEN, Microcraters on Lunar Rocks. *Proc. Third Lunar Science Conference, Geochimica et Cosmochimica Acta*, Supplement 3, Vol. 3, 1972, pp. 2767-2791.
 22. GAULT, D. E., Saturation and Equilibrium Conditions for Impact Cratering on the Lunar Surface: Criteria and Implications. *Radio Science*, Vol. 5, 1970, pp. 272-291.
 23. STORZER, D., G. POUPEAU, AND W. KRÄTSCHMER, Track Exposure and Formation Ages of Some Lunar Samples. *Proc. Fourth Lunar Science Conference, Geochimica et Cosmochimica Acta*, Supplement 4, Vol. 3., 1973, pp. 2363-2377.
 24. STORZER, D., AND G. A. WAGNER, Correction of Thermally Lowered Fission Track Ages of Tektites. *Earth Planet. Sci. Letters*, Vol. 5, 1969, pp. 463-468.
 25. CROZAZ, G., AND R. M. WALKER, Solar Particle Tracks in Glass From Surveyor 3 Spacecraft. *Science*, Vol. 171, 1971, pp. 1237-1239.
 26. FLEISCHER, R. L., H. R. HART, AND G. M. COMSTOCK, Very Heavy Solar Cosmic Rays: Energy Spectrum and Implications for Lunar Erosion. *Science*, Vol. 171, 1971, pp. 1240-1242.
 27. BARBER, J., R. COWSIK, I. R. HUTCHEON, P. B. PRICE, AND R. S. RAJAN, Solar Flares, the

- Lunar Surface and Gas-Rich Meteorites. *Proc. Second Lunar Science Conference, Geochimica et Cosmochimica Acta*, Supplement 2, Vol. 3, 1971, pp. 2705-2714.
28. FLEISCHER, R. L., H. R. HART, JR., G. M. COMSTOCK, AND A. O. EVWARAYE, The Particle Track Record of the Ocean of Storms. *Proc. Second Lunar Science Conference, Geochimica et Cosmochimica Acta*, Supplement 2, Vol. 3, 1971, pp. 2559-2568.
 29. BHANDARI, N., S. BHAT, D. LAL, G. RAJAGOPALAN, A. S. TAMHANE, AND V. S. VENKATAVARADAN, High Resolution Time Averaged (Millions of Years) Energy Spectrum and Chemical Composition of Iron-Group Cosmic Ray Nuclei at 1 A.U. Based on Fossil Tracks in Apollo Samples. *Proc. Second Lunar Science Conference, Geochimica et Cosmochimica Acta*, Supplement 2, Vol. 3, 1971, pp. 2611-2619.
 30. CROAZ, G., R. WALKER, AND D. WOOLUM, Nuclear Track Studies of Dynamic Surface Processes on the Moon and the Constancy of Solar Activity. *Proc. Second Lunar Science Conference, Geochimica et Cosmochimica Acta*, Supplement 2, Vol. 3, 1971, pp. 2543-2558.
 31. HART, H. R., JR., G. M. COMSTOCK, AND R. L. FLEISCHER, The Particle Track Record of Fra Mauro. *Proc. Third Lunar Science Conference, Geochimica et Cosmochimica Acta*, Supplement 3, Vol. 3, 1972, pp. 2831-2844.
 32. BHANDARI, N., J. N. GOSWAMI, S. K. GUPTA, D. LAL, A. S. TAMHANE, AND V. S. VENKATAVARADAN, Collision Controlled Radiation History of the Lunar Regolith. *Proc. Third Lunar Science Conference, Geochimica et Cosmochimica Acta*, Supplement 3, Vol. 3, 1972, pp. 2811-2819.
 33. YUHAS, D., Personal communication, 1973.
 34. BHANDARI, N., J. GOSWAMI, AND D. LAL, Surface Irradiation and Evolution of the Lunar Regolith. *Proc. Fourth Lunar Science Conference, Geochimica et Cosmochimica Acta*, Supplement 4, Vol. 3, 1973, pp. 2275-2290.
 35. BERG, O. E., AND E. GRÜN, Evidence of Hyperbolic Cosmic Dust Particles. *Space Research*, Vol. XIII, Akademie-Verlag, Berlin, 1973, pp. 1047-1055.
 36. ZOOK, H. A., AND O. E. BERG, A Source for Hyperbolic Cosmic Dust Particles. Presented at COSPAR, Konstanz, 1973; submitted for publication to *Planet. and Space Sci.*, 1974.
 37. WYATT, J. S. P., AND F. C. WHIPPLE, The Poynting-Robertson Effect on Meteor Orbits. *Astrophys. J.*, Vol. 11, 1950, pp. 134-141.
 38. HEMENWAY, C. L., D. S. M. HALLGREN, AND D. C. SCHMALBERGER, Stardust. *Nature*, Vol. 238, 1972, pp. 256-260.
 39. HOFFMANN, H.-J., H. FECHTIG, E. GRÜN, AND J. KISSEL, First Results of the Micrometeoroid Experiment S215 on the HEOS 2 Satellite. Presented at COSPAR, Konstanz, 1973; submitted for publication to *Planet. and Space Sci.*, 1974.
 40. HOFFMANN, H.-J., H. FECHTIG, E. GRÜN, AND J. KISSEL, Temporal Fluctuations and Anisotropy of the Micrometeoroid Flux in the Earth-Moon System Measured by HEOS 2. Presented at COSPAR, Sao Paolo, 1974; submitted for publication to *Planet. and Space Sci.*
 41. BERG, O. E., AND U. GERLOFF, More Than Two Years of Micrometeorite Data From Two Pioneer Satellites. *Space Res.*, Vol. XI, Akademie-Verlag, Berlin, 1971, pp. 225-235.
 42. HARTUNG, J. B., D. STORZER, AND F. HÖRZ, Toward a Lunar Microcrater Clock. *Lunar Science*, Vol. V Abstracts, 1974, pp. 307-309.
 43. SCHNEIDER, E., AND F. HÖRZ, Lunar Rock Erosion. *Lunar Science*, Vol. V Abstracts, Lunar Science Institute, Houston, 1974, pp. 666-668.
 44. GAULT, D. E., Displaced Mass, Depth, Diameter and Effects of Oblique Trajectories for Impact Craters Formed in Dense Crystalline Rocks. *The Moon*, Vol. 6, 1973, pp. 32-44.
 45. MEHL, A., Investigation on the Chemical Modification in an Impact Crater on a Lunar Sample. *Space Research*, Vol. XIV, Akademie-Verlag, Berlin, 1974, pp. 741-743.